

Efficient chip-based optical parametric oscillators from 590 nm to 1150 nm

Jordan R. Stone,^{1,2,*} Xiyuan Lu,^{1,2} Gregory Moille,^{1,2} and Kartik Srinivasan^{1,2}

¹*Joint Quantum Institute, NIST/University of Maryland, College Park, MD 20742*

²*National Institute for Standards and Technology, Gaithersburg, MD 20899*

(Dated: August 17, 2022)

Optical parametric oscillators are widely used to generate coherent light at frequencies not accessible by conventional laser gain. However, chip-based parametric oscillators operating in the visible spectrum have suffered from pump-to-signal conversion efficiencies typically less than 0.1 %. Here, we demonstrate efficient optical parametric oscillators based on silicon nitride photonics that address frequencies between 260 THz (1150 nm) and 510 THz (590 nm). Pumping silicon nitride microrings near 385 THz (780 nm) yields monochromatic signal and idler waves with unprecedented output powers in this wavelength range. We estimate on-chip output powers (separately for the signal and idler) between 1 mW and 5 mW and conversion efficiencies reaching ≈ 15 %. Underlying this improved performance is our development of pulley waveguides for broadband near-critical coupling, which exploits a fundamental connection between the waveguide-resonator coupling rate and conversion efficiency. Finally, we find that mode competition reduces conversion efficiency at high pump powers, thereby constraining the maximum realizable output power. Our work proves that optical parametric oscillators built with integrated photonics can produce useful amounts of visible laser light with high efficiency.

I. INTRODUCTION

Lasers operating at visible and near-infrared (NIR) wavelengths are essential to modern science and technology [1–4], but affordable systems typically suffer from poor spectral purity and gaps in spectral coverage, while higher-performance options are large and expensive. The latter often rely on bulk nonlinear optics to spectrally translate longer-wavelength lasers to the targeted frequency, employing either sum-frequency or second-harmonic generation in $\chi^{(2)}$ -nonlinear media [5–7]. Their operational complexity and substantial power consumption (they often require liquid cooling systems) renders them impractical in many situations. Hence, it is desirable to transition the nonlinear wavelength conversion to a more scalable nonlinear optics platform, e.g., integrated photonics.

One approach is to leverage the wavelength flexibility inherent to optical parametric oscillators using nonlinear microresonators, which possess large optical quality factors (Q) and small mode volumes to intensify circulating light and promote efficient nonlinear interactions [8, 9]. Recent studies of microresonator-based optical parametric oscillators (μ OPOs) have demonstrated broad spectral separation between pump and generated light [10–12], low-power operation [13, 14], and visible-wavelength access [15]. While both $\chi^{(2)}$ and $\chi^{(3)}$ μ OPOs offer some wavelength flexibility, $\chi^{(3)}$ systems are useful to generate visible light from a NIR pump; moreover, their natural availability in the popular silicon photonics platform [16] can enable their scalable fabrication and integration with other components, including pump lasers [17]. On the other hand, the reported or inferred (e.g., from optical

spectra) conversion efficiencies are $\lesssim 0.1\%$ [10, 13, 15, 18–20], and the available output power is far too low for many applications (e.g., $<10 \mu\text{W}$ for previous visible μ OPOs [15]). Realizing higher conversion efficiencies and output powers would enable a wide range of on-chip applications and broaden the reach of silicon photonics in the visible spectrum.

Here, we demonstrate efficient μ OPOs that generate coherent light within the spectral window between 260 THz and 510 THz (590 nm and 1150 nm). We measure conversion efficiencies between 3.5 % and 14.5 % with corresponding on-chip output powers greater than 1 mW (and as high as 5 mW). Our results spring from efficient broadband waveguide-resonator coupling, which we realize with pulley-waveguide geometries designed using coupled-mode simulations. In the rest of this paper, we first introduce the key μ OPO physics and specify our experimental procedures. Then, we explain our coupled-mode simulations and present measurements to confirm their accuracy. Next, we present the optical spectra of 16 different μ OPOs, from which we determine output powers and conversion efficiencies. Finally, we show how parasitic nonlinear processes currently constrain the maximum realizable output power. Our work is an important step forward in the quest for practical, chip-based sources of visible laser light using nonlinear optics.

The μ OPOs we consider generate monochromatic signal and idler waves from a continuous-wave (CW) pump laser through resonantly-enhanced degenerate four wave mixing (FWM), as depicted in Fig. 1a [21]. In experiments, we pump a fundamental transverse-electric (TE1) eigenmode of a silicon nitride microring near 385 THz, and FWM transfers energy to TE1 signal and idler modes. In principle, the range of accessible output frequencies, as constrained only by energy conservation, is DC to $2\omega_p$, where ω_p is the pump frequency. However, in practice this range is dictated by the group veloc-

* jstone12@umd.edu

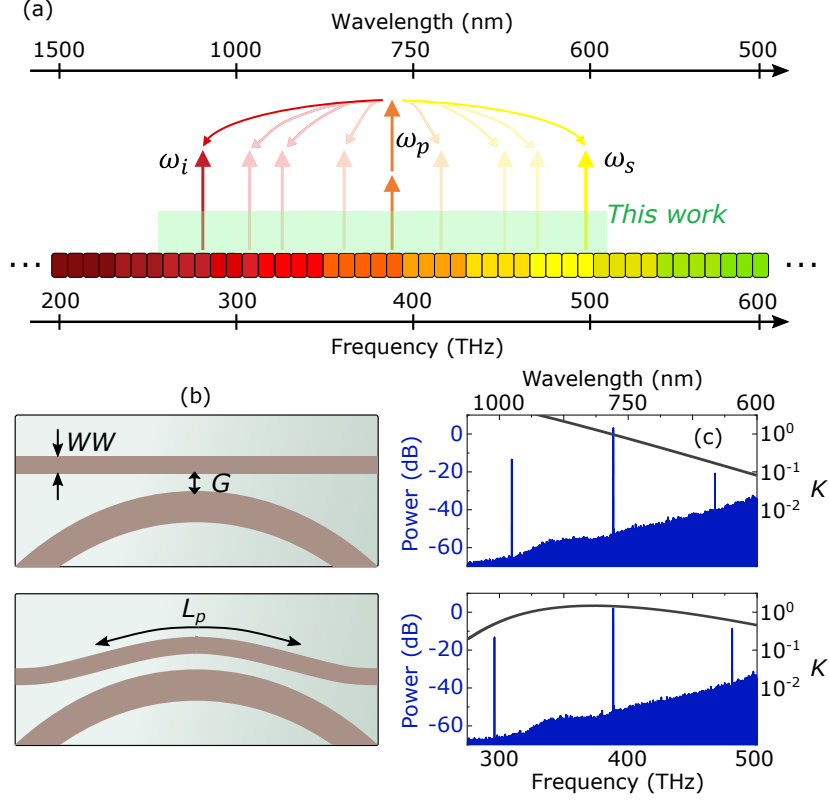


FIG. 1. **Achieving high conversion efficiency (CE) across a wide spectral band with microresonator-based optical parametric oscillators (μ OPOs).** (a) Conceptual depiction of $\chi^{(3)}$ optical parametric oscillation. Two pump photons (frequency ω_p) are converted to one signal (ω_s) photon and one idler (ω_i) photon. We focus on generating different μ OPOs (faded arrows) within the spectral window between 260 THz and 510 THz, as marked by the green stripe. (b) Depictions of microring couplers, as viewed from above, which rely on evanescent coupling between the microring and either a straight access waveguide (top panel) or a pulley waveguide (bottom panel). Couplers are defined by three geometric parameters: the waveguide width, WW , the gap (or distance) between the microring and waveguide, G , and the length of waveguide, L_p , that runs parallel to the microring. (c) Simulated coupling ratios, K (gray), and measured μ OPO spectra (blue) for identical microrings with different coupling geometries. The top panel data corresponds to a straight waveguide ($WW = 375$ nm; $G = 125$ nm) coupler, while bottom panel data corresponds to a pulley waveguide (same WW and G ; $L_p = 3$ μ m).

ity dispersion (GVD), which must be engineered such that FWM to the targeted signal and idler modes is favored (simultaneously phase- and frequency-matched), but FWM to other modes is suppressed. In Appendix A, we recount our approach to dispersion engineering that is also described in Ref. 15.

A separate challenge is to ensure that pump power is efficiently converted into output signal or idler power. Hence, we define the on-chip conversion efficiency as:

$$CE = \frac{P_{s(i)}}{P_{in}}, \quad (1)$$

where $P_{s(i)}$ is the signal (idler) power in the waveguide output, and P_{in} is the pump power in the waveguide input. Recent theoretical work has derived the maximum obtainable CE as:

$$CE_{s(i)}^{\max} = \frac{1}{2} \frac{\kappa_{s(i)} \kappa_p}{\Gamma_{s(i)} \Gamma_p} \frac{\omega_{s(i)}}{\omega_p}, \quad (2)$$

where $\kappa_{s(i)}$ and κ_p are the waveguide-resonator coupling rates of the signal (idler) and pump modes, $\Gamma_{s(i)}$ and Γ_p are the total loss rates (i.e., loaded linewidths) of the signal (idler) and pump modes, and $\omega_{s(i)}$ and ω_p are the frequencies of the signal (idler) and pump light, respectively [10]. Clearly, obtaining large CE involves engineering κ for both the pump mode and targeted signal/idler modes. Such coupling engineering is a common problem in the nonlinear optics of Kerr microresonators; it arises, for example, in the efficient extraction of octave-spanning Kerr microcombs [22]. The problem is that, given a straight waveguide evanescently coupled to a microring resonator, κ decreases exponentially with frequency due to decreasing overlap of the microring mode with the waveguide mode. Hence, when the pump mode is criti-

cally coupled, the signal mode is undercoupled, resulting in low CE . Moreover, when ω_s is a visible frequency, the smaller evanescent decay length compared to NIR frequencies exacerbates the challenge. One solution is to utilize so-called pulley waveguides, which increase the physical distance over which the waveguide and microring can exchange energy [22, 23]. Figure 1b illustrates the physical differences between straight-waveguide couplers (top panel) and pulley-waveguide couplers (bottom panel), and it depicts the three geometric parameters that define such couplers in our study: The waveguide width, WW , the waveguide-resonator gap, G , and the pulley length, L_p (which approaches zero in the straight-waveguide limit). In Fig. 1c, we present measurements of μ OPO spectra extracted from nominally identical microrings using either a straight-waveguide coupler (top panel) or a pulley-waveguide coupler (bottom panel). These measurements are representative of other comparisons between the two coupling schemes. While P_i is roughly the same in each case, P_s is approximately $20\times$ greater in the pulley waveguide. To explain the result, we show in the same panels the simulated coupling ratio, defined as $K = \kappa/\gamma$, where $\gamma = \Gamma - \kappa$ is the intrinsic loss rate. Near ω_s , K is $\approx 8\times$ higher for the pulley-waveguide coupler.

II. DESIGN AND TEST OF WAVEGUIDE COUPLERS

To design couplers for testing, we simulate κ spectra for a variety of coupling geometries with the goal of achieving $K \approx 1$ (i.e., critical coupling) at frequencies between 260 THz and 510 THz. Notably, achieving high CE only requires that κ be optimized at ω_p and either ω_s or ω_i , depending on which output wave (signal or idler) is to be used. (Moreover, ideally, the unused wave is undercoupled to reduce threshold power). At the same time, broadband near-critical coupling is preferable, since then a single coupling geometry is robust against design imperfections, and it may be used for many different μ OPOs. Our simulations are based on a coupled mode theory for optical waveguides [24], which calculates κ according to:

$$\kappa = \frac{c}{2\pi R n_g} |k_t|^2, \quad (3)$$

where R is the microring outer radius, c is the speed of light, n_g is the group refractive index, and k_t is a coupling coefficient defined as:

$$k_t = \frac{i\omega}{4} \int_L \left[\int_A (\epsilon_{WG} - \epsilon_R) \mathbf{E}_R^* \cdot \mathbf{E}_{WG} dr dz \right] e^{i\phi} dl, \quad (4)$$

where $\epsilon_{WG(R)}$ is the dielectric permittivity of the access waveguide (microring), $\mathbf{E}_{WG(R)}$ is the electric field of the waveguide (microring) eigenmode, and ϕ is an accumulated phase accounting for the difference in the waveguide

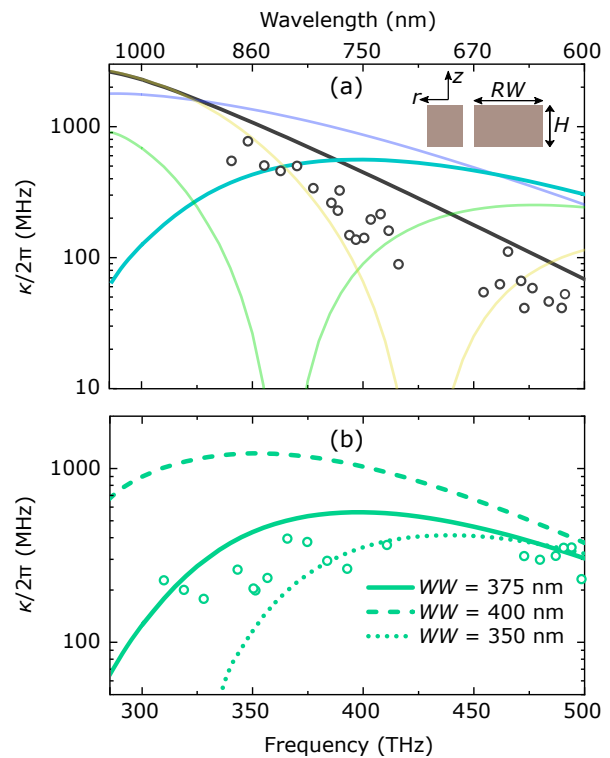


FIG. 2. **Design, simulation, and measurement of coupling rate (κ).** (a) Simulated κ spectra for a silicon nitride (SiN) microring with waveguide parameters $WW = 375$ nm, $G = 150$ nm, and $L_p = 0$ μ m (bold gray curve), 2 μ m (faded blue), 3 μ m (bold turquoise), 4 μ m (faded green), and 5 μ m (faded yellow). The circular data points indicate measured κ values for the coupler with $L_p = 0$ μ m. The inset depicts the waveguide/microring cross section, including labels for the ring width (RW) and height (H), and shows axes for the coordinates r and z over which we integrate Eq. 4. (b) Simulated κ spectra for a SiN microring with waveguide parameters $G = 150$ nm, $L_p = 3$ μ m, and different values of WW . The circular data points indicate measured κ values for the coupler with $WW = 375$ nm. The uncertainty in the measured κ values as determined from a nonlinear least squares fit to the resonator transmission spectrum is smaller than the data point size.

and microring propagation constants. The coordinates r and z are horizontal and vertical coordinates in-plane with the microring/waveguide cross section, as labeled in the Fig. 2a inset, and l follows the direction of light propagation. The central integral in Eq. (4) evaluates the evanescent overlap between the microring and waveguide modes at the frequency ω . For more details, see Ref. [22]. Figure 2a shows simulated κ spectra for a SiN microring with nominal $R = 25$ μ m, ring width $RW = 825$ nm, and height $H = 500$ nm, which are chosen to suitably engineer the GVD (see Appendix A). In addition, we choose $WW = 375$ nm, $G = 150$ nm, and L_p from 0 μ m (i.e., a straight-waveguide coupler) to 5 μ m. Increasing L_p results in larger κ at higher frequencies compared to the straight-waveguide coupler (dark grey line), but it introduces resonances in the κ spectra (i.e., regions where

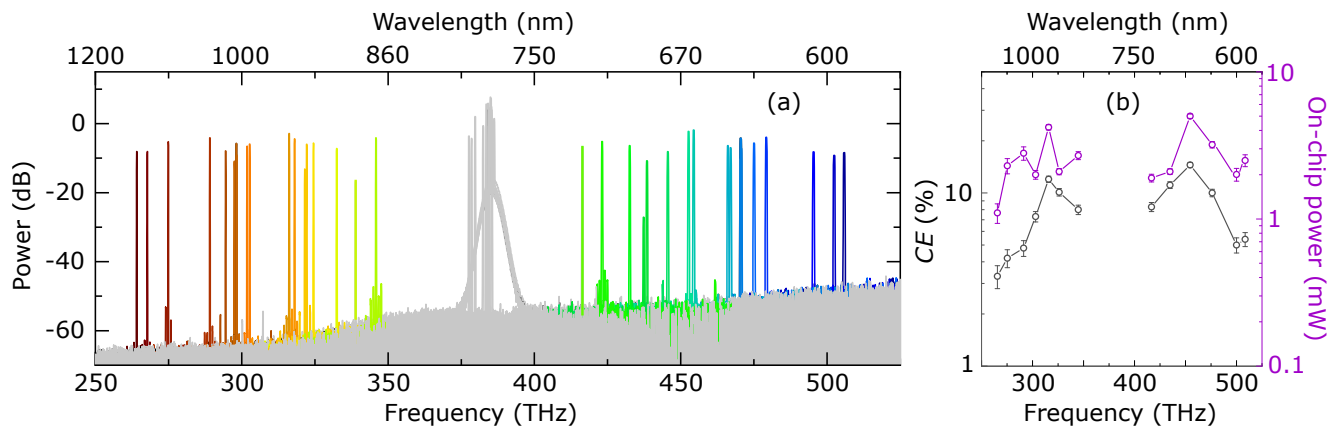


FIG. 3. μ OPO spectra, conversion efficiency, and output power. (a) μ OPO spectra from a series of devices recorded with an optical spectrum analyzer (OSA). Here, the y axis is normalized such that 0 dB is equal to 1 mW. No correction factors (e.g., from optical losses) are applied to these data. The transmitted pump light is shown in gray, and the signal/idler light is shown in color. (b) CE (gray) and P_i or P_s (purple; left and right portions of data, respectively) versus frequency, taking into account optical losses between the waveguide and OSA (see Appendix B). Error bars are estimated from the precision uncertainties in our measurements of optical power.

$\kappa \rightarrow 0$) that arise from the coherent energy exchange between the microring and waveguide. These resonances blueshift when L_p is increased. Based on these data, we select $L_p = 3 \mu\text{m}$ for further study because it minimizes variations in κ over the targeted spectral region.

Next, we optimize WW and G . The predominant effect of changing G is to vertically shift the entire κ spectrum; i.e., G has little impact on the spectral location of the coupling resonances. However, the relationship between κ and WW is more complex. Within the range of values considered, larger WW increases κ because the waveguide propagation constant shifts closer to the microring propagation constant, and the evanescent overlap between the microring and waveguide modes is not appreciably changed. At the same time, coupling resonances are redshifted. Figure 2b shows κ spectra for $G = 150$ nm, $L_p = 3 \mu\text{m}$, and three values of WW . Apparently, the flattest κ spectra are realized for WW between 375 and 400 nm. After choosing WW , G may be chosen to realize critical coupling near ω_p .

To assess the accuracy of our simulations, we fabricate an array of SiN microrings with systematic coupling parameter variations (see Appendix C for details on our fabrication process), and we measure κ for each device. Specifically, we use either $L_p = 0$ or $L_p = 3 \mu\text{m}$, G between 110 nm and 160 nm, and WW between 350 nm and 400 nm. To measure κ , we carry out mode spectroscopy using a CW Titanium Sapphire (TiS) laser, which is tunable from 305 THz to 415 THz (720 nm to 980 nm). In addition, we can perform sum frequency generation with the TiS laser and a 154 THz (1950 nm) laser to generate coherent light from 460 THz to 510 THz (590 nm to 650 nm). We find that simulations predict slightly larger κ values than we measure; to compensate, we reduce G by approximately 20 nm in experiments. In Fig. 2a, we present κ measurements (gray circles) of a

straight-waveguide-coupled device with $WW = 375$ nm and $G = 125$ nm. The measured κ values are slightly lower than the corresponding simulation with $G = 150$ nm, but both data decrease exponentially with frequency, which is a known characteristic of straight-waveguide couplers [22]. Specifically, we measure $\kappa \approx 800$ MHz near 350 THz, but it drops sharply to $\kappa \approx 40$ MHz near 500 THz. In contrast, we observe a more achromatic κ spectrum in a pulley-waveguide-coupled device with $WW = 375$ nm, $G = 135$ nm, and $L_p = 3 \mu\text{m}$. Our measurements (green circles) are shown in Fig. 2b, and they agree with the corresponding simulation with $G = 150$ nm. Our measurements indicate that, between 300 THz and 500 THz, κ takes on values over the relatively narrow range (compared to the straight-waveguide coupler) of 180 MHz to 400 MHz. We also measure $\gamma \approx 300$ MHz that is approximately independent of optical frequency. Therefore, according to Eq. 2, our best pulley-waveguide-coupled devices should support many different μ OPOs with $CE > 1\%$.

III. μ OPO GENERATION AND CONVERSION EFFICIENCY MEASUREMENTS

To test our prediction, we record μ OPO spectra with a calibrated optical spectrum analyzer (OSA) and calculate P_s , P_i , and CE values after accounting for optical losses between the waveguide and OSA (for details, see Appendix B). To generate μ OPOs, we tune ω_p into resonance, starting blue detuned and decreasing ω_p until P_s and P_i are maximized. We repeat this procedure for different P_{in} values with the goal of maximizing CE . To ensure a variety of $\omega_{s(i)}$ values, we engineer the GVD by systematically varying RW in different devices (see Ref. [15] and Appendix A). We utilize pulley-waveguide

couplers such as those characterized in Fig. 2, and we find that CE is maximized for $L_p = 3 \mu\text{m}$, WW between 375 nm and 400 nm, and G between 125 nm and 135 nm. In Fig. 3a, we present a compiled set of μOPO spectra that we extract from pulley-waveguide couplers with parameters in the above optimum range. In most cases, both P_s and P_i are greater than 1 mW, and P_{in} is typically between 30 mW and 45 mW. However, there are atypical μOPO spectra for which either P_s or P_i is $\ll 1$ mW. Most likely, these result from mode interactions that locally alter the microring GVD and Q [25, 26]. Table II in Appendix B lists the individual pump, signal, and idler frequencies and powers for each μOPO spectrum shown in Fig. 3(a).

To characterize the μOPO performance, we calculate from Fig. 3a the largest values of P_s and P_i in spectral bins spanning approximately 20 THz each, and we plot the results in Fig. 3b along with the corresponding CE values. We find $P_i > 1$ mW from 264 THz to 346 THz and $P_i > 2$ mW from 275 THz to 346 THz. In the best case, we generate 4 mW of idler power at 315 THz using $P_{\text{in}} = 34$ mW, which equates to $CE \approx 12\%$. Meanwhile, $P_s > 1.9$ mW from 416 THz to 506 THz, and in the best case, we generate 5 mW of signal power at 454 THz using $P_{\text{in}} = 34$ mW, which equates to $CE \approx 14.5\%$. Moreover, as expected from our simulations and measurements of κ and Eq. 2, CE decreases in the spectral wings as a result of smaller κ .

IV. LIMITATIONS ON OUTPUT POWER

Finally, we discuss the limits to μOPO output power and analyze an example. The relationship between $P_{s(i)}$, P_{in} , and other experimental parameters has been analyzed theoretically [27]. Therein, it was predicted that $P_{s(i)}$ increases with P_{in} for $P_{\text{in}} \gtrsim P_{\text{th}}$, but further increases in P_{in} lead to saturation or even reduction of $P_{s(i)}$. The reason is that parasitic FWM processes compete with the targeted μOPO process. The predominant parasitic FWM process that we observe in experiments is mode competition between the targeted signal/idler modes and their spectral neighbors [27]. In Fig. 4, we show the μOPO spectrum for a single device as P_{in} is increased. For $P_{\text{in}} = 32$ mW, only the pump, signal, and idler modes oscillate, and $P_{s(i)} > 1$ mW (top panel). The idler power in this case is marked by the red line in each panel. When $P_{\text{in}} = 50$ mW (middle panel), ω_s and ω_i shift to higher and lower frequencies, respectively. This behavior was predicted in Ref. [27] and termed ‘mode switching.’ In addition, other modes with frequencies close to $\omega_{s(i)}$ begin to oscillate and steal energy from the μOPO . Hence, P_i decreases to a level below the red line, despite the increase in P_{in} . When P_{in} is further increased to 70 mW (bottom panel), $P_{s(i)}$ remains approximately the same, but the power in the competing modes increases. The behavior demonstrated in this example is ubiquitous within our μOPO devices

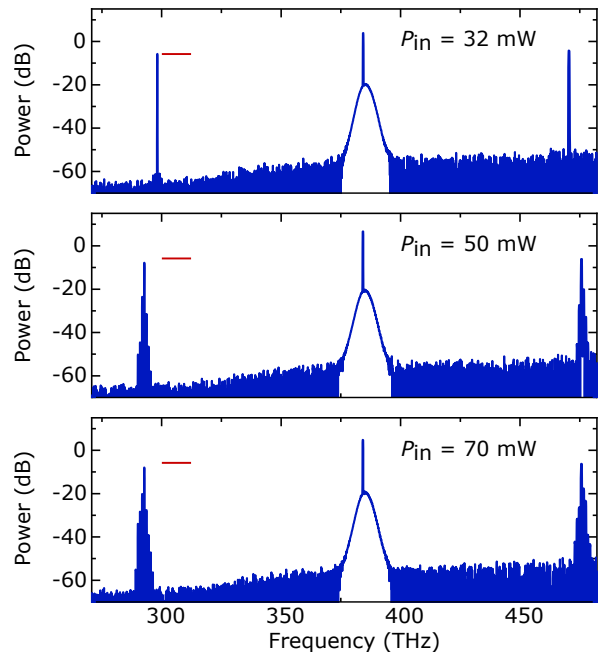


FIG. 4. **Mode competition constrains the μOPO output power.** The figure depicts μOPO spectra at three different pump powers, P_{in} . For $P_{\text{in}} = 32$ mW (top panel), only the pump, signal, and idler modes oscillate. As P_{in} is increased (middle and bottom panels), mode switching occurs, and mode competitions distribute energy to modes other than the targeted signal/idler pair, leading to reduced $P_{s(i)}$. To guide the eye, we include a red line in each panel that marks the top-panel P_i level.

and explains why $P_{s(i)}$ cannot be increased arbitrarily by increasing P_{in} . Still, increasing CE and $P_{s(i)}$ beyond the levels we demonstrate may be possible using alternate phase- and frequency-matching strategies, such as that reported in Ref. [28]. As it stands, the achieved power levels are relevant for some applications, such as spectroscopy of various coherent near-infrared and visible systems [29, 30].

V. DISCUSSION

In conclusion, we have demonstrated energy-efficient μOPO s with practically-relevant output powers in a crucial portion of the visible and near-infrared spectrum. Our results are enabled by broadband pulley-waveguide couplers that we design using coupled-mode simulations. For the most widely-separated μOPO s, we observe relatively lower CE values that are consistent with under-coupled signal and idler modes. Hence, an important focus for future work is to extend the spectral bandwidth over which devices are nearly critically coupled, thus broadening the range of frequencies that can be efficiently extracted into a single waveguide. Other possible approaches include using frequency-specific coupling geometries (e.g., one may optimize κ at the μOPO -specific

frequencies ω_s and ω_p , while neglecting the idler), or to couple multiple waveguides - each designed for different portions of the μ OPO spectrum - to one microring. Moreover, new strategies should be devised to avoid parasitic FWM processes and increase the realizable output power. Nonetheless, our work is a compelling demonstration that μ OPOs can help satisfy the demand for compact sources of visible laser light.

ACKNOWLEDGMENTS

We thank Khoi Hoang and Tahmid Sami Rahman for carefully reading the manuscript and giving useful feedback. This project is funded by the DARPA LUMOS and NIST-on-a-chip programs.

Appendix A: Engineering GVD to control the μ OPO spectrum

The microresonator GVD determines which frequencies, if any, are phase- and frequency-matched for FWM. When designing $\chi^{(3)}$ μ OPOs, a convenient quantity related to GVD is the frequency mismatch parameter, $\delta(\nu) = \nu_s + \nu_i - 2\nu_p$, where we use a slightly different notation than in the main text; namely, $\nu_{s(i)}$ are the set of possible signal (idler) mode frequencies, and ν_p is the pump mode frequency. Degenerate FWM is allowed when $\delta(\nu) \gtrsim 0$ (small positive δ is required to compensate nonlinear shifts). Figure 5a shows a typical $\delta(\nu)$ spectrum as engineered for a $\chi^{(3)}$ μ OPO system. The spectrum exhibits normal dispersion around ν_p , which is necessary to suppress comb formation [15], and higher-order GVD causes δ to turn and pass through zero [27]. In general, oscillation occurs on the mode pair with smallest positive δ .

The δ spectrum is controlled through the microring geometry; namely, the RW parameter. Moreover, a given microring may support several different μ OPOs, depend-

ing on ω_p . In our devices, a group of four or five pump modes will yield different μ OPO spectra, with larger ω_p increasing the signal-idler frequency separation. In Fig. 5b, we mark ω_p , ω_s , and ω_i for four different μ OPOs at each of three RW values. Importantly, fine-tuning RW (combined with a strategic choice of ω_p) can yield μ OPOs with generated frequencies anywhere in the targeted spectral window.

Appendix B: Estimating on-chip powers from OSA measurements

Future integrated-photonics systems will route laser light from source to destination (e.g., from a μ OPO-generating microring to an integrated atomic vapor cell) via low-loss optical waveguides. Hence, we estimate on-chip powers and conversion efficiencies, which requires a careful calibration of optical losses between the waveguide and OSA. In general, such losses are dispersive, so we measure them for each device at a comprehensive set of optical frequencies. We use lensed fibers to in- and out-couple light to and from the waveguide. The lensed-fiber output is split using a fiber-based 90/10 coupler that is designed for a wide wavelength span around 780 nm. The ‘90’ output port is connected to the OSA via optical fiber, while light from the other port is connected to a photodetector. To estimate losses, we use a power meter to record the optical power at various points in the experiment; specifically, we take measurements at the lensed-fiber input, lensed-fiber output, and OSA input. Finally, we note any discrepancies between the OSA input and OSA reading. Table II shows an example taken at 306 THz (980 nm) for one μ OPO device. Adding the different losses yields the OSA-to-on-chip power conversion factor, which allows us to convert μ OPO spectra to on-chip signal/idler powers. Moreover, knowledge of the waveguide-to-lensed-fiber coupling losses allows us to estimate the on-chip pump power in experiments, which we use to estimate CE values.

Measurement point	Power (μ W)	Loss (dB)
Input to waveguide	10	N/A
Output from waveguide	2.2	3.3 per waveguide facet
Input to OSA (after coupler)	1.4	2
OSA reading	0.7	3
Total		8.3

TABLE I. Example of loss calibrations at 306 THz (980 nm) to determine the on-chip power conversion factor.

Finally, we tabulate the signal and idler frequencies

and on-chip powers for each of the 16 spectra shown in

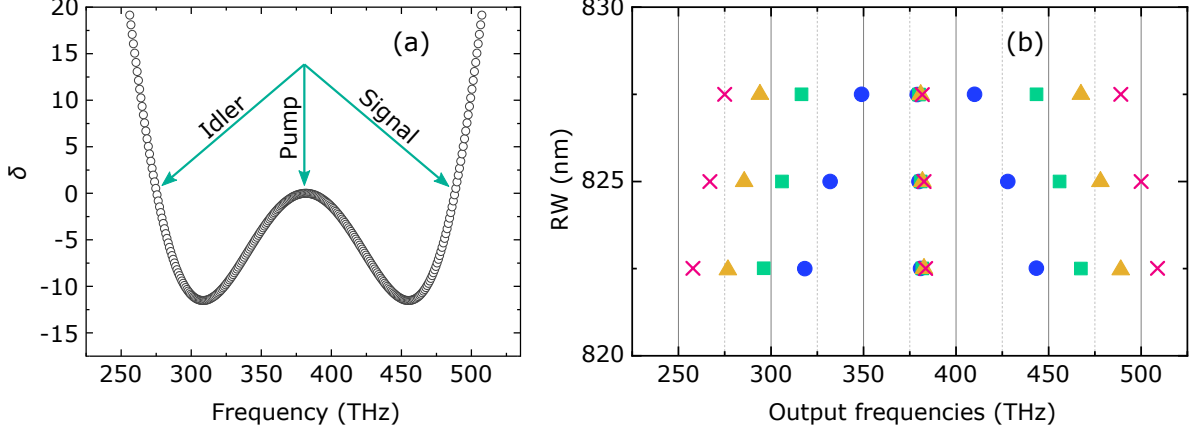


FIG. 5. **Engineering dispersion in μ OPO systems.** (a) Simulated frequency mismatch parameter, δ , versus frequency. Arrows point to the generated frequencies, ω_s and ω_i , and the pump frequency, ω_p . (b) Predicted μ OPO frequencies for different values of RW and ω_p . Different colors/shapes correspond to different pump modes, with ω_p (near 385 THz) increasing from the blue circle to the red cross.

Fig. 3a. These data are presented in

$\omega_p/2\pi$ (THz)	P_{in} (mW)	$\omega_s/2\pi$ (THz)	P_s (mW)	$\omega_i/2\pi$ (THz)	P_i (mW)
385	34	423	2.2	346	2.7
378	26	416	1.8	339	0.2
378	20	432	1.8	324	2.1
380	25	437	0.02	322	1.8
385	27	438	0.8	332	1.4
384	30	446	1.3	321	0.4
385	36	454	5.0	318	2.6
385	35	454	4.4	316	4.0
384	28	466	1.9	303	1.8
384	46	467	1.7	302	1.6
384	32	470	3.3	298	1.9
386	33	475	2.2	297	0.6
384	59	479	3.4	289	2.7
385	55	495	2.4	275	2.3
385	34	502	2.0	268	1.1
385	47	506	2.5	264	1.1

TABLE II. Pump, signal, and idler frequencies and on-chip powers for the 16 μ OPO spectra presented in Fig. 3a.

Appendix C: Fabrication methods

To create device layouts, we use the Nanolithography Toolbox, a free software package developed by NIST [31]. We deposit stoichiometric SiN (Si_3N_4) by low-pressure

chemical vapor deposition on top of a 3 μm -thick layer of SiO_2 on a 100 mm diameter Si wafer. We fit ellipsometer measurements of the wavelength-dependent SiN refractive index and layer thicknesses to an extended Sellmeier model. The device pattern is created in positive-tone re-

sist by electron-beam lithography and then transferred to SiN by reactive ion etching using a CF_4/CHF_3 chemistry. After cleaning the devices, we anneal them for four hours at 1100°C in N_2 . Next, we perform oxide lift-off to make

devices air-clad around their left, right, and top sides. The facets of the chip are then polished for lensed-fiber coupling. After polishing, the chip is annealed again.

-
- [1] Tobias Bothwell, Colin J Kennedy, Alexander Aepli, Dhruv Kedar, John M Robinson, Eric Oelker, Alexander Staron, and Jun Ye, “Resolving the gravitational redshift across a millimetre-scale atomic sample,” *Nature* **602**, 420–424 (2022).
- [2] David Awschalom, Karl K Berggren, Hannes Bernien, Sunil Bhave, Lincoln D Carr, Paul Davids, Sophia E Economou, Dirk Englund, Andrei Faraon, Martin Fejer, *et al.*, “Development of quantum interconnects (quics) for next-generation information technologies,” *PRX Quantum* **2**, 017002 (2021).
- [3] Luiz Eduardo Mendes Matheus, Alex Borges Vieira, Luiz FM Vieira, Marcos AM Vieira, and Omprakash Gnawali, “Visible light communication: concepts, applications and challenges,” *IEEE Communications Surveys & Tutorials* **21**, 3204–3237 (2019).
- [4] Ralph Weissleder, “A clearer vision for in vivo imaging,” *Nature Biotechnology* **19**, 316–317 (2001).
- [5] Jonathan N Tinsley, Satvika Bandarupally, Jussi-Pekka Penttinen, Shamaila Manzoor, Sanna Ranta, Leonardo Salvi, Mircea Guina, and Nicola Poli, “Watt-level blue light for precision spectroscopy, laser cooling and trapping of strontium and cadmium atoms,” *Optics Express* **29**, 25462–25476 (2021).
- [6] Daniele C Parrotta, Alan J Kemp, Martin D Dawson, and Jennifer E Hastie, “Multiwatt, continuous-wave, tunable diamond raman laser with intracavity frequency-doubling to the visible region,” *IEEE Journal of Selected Topics in Quantum Electronics* **19**, 1400108–1400108 (2013).
- [7] Richard P Mildren, Helen M Pask, Hamish Ogilvy, and James A Piper, “Discretely tunable, all-solid-state laser in the green, yellow, and red,” *Optics Letters* **30**, 1500–1502 (2005).
- [8] Kerry J Vahala, “Optical microcavities,” *Nature* **424**, 839–846 (2003).
- [9] TJ Kippenberg, SM Spillane, and KJ Vahala, “Kerr-nonlinearity optical parametric oscillation in an ultrahigh-q toroid microcavity,” *Physical Review Letters* **93**, 083904 (2004).
- [10] Noel Lito B Sayson, Toby Bi, Vincent Ng, Hoan Pham, Luke S Trainor, Harald GL Schwefel, Stéphane Coen, Miro Erkintalo, and Stuart G Murdoch, “Octave-spanning tunable parametric oscillation in crystalline kerr microresonators,” *Nature Photonics* **13**, 701–706 (2019).
- [11] Christoph Sebastian Werner, Tobias Beckmann, Karsten Buse, and Ingo Breunig, “Blue-pumped whispering gallery optical parametric oscillator,” *Optics Letters* **37**, 4224–4226 (2012).
- [12] Yuechen Jia, Kevin Hanka, Kevin T Zawilski, Peter G Schunemann, Karsten Buse, and Ingo Breunig, “Continuous-wave whispering-gallery optical parametric oscillator based on cdsip2,” *Optics Express* **26**, 10833–10841 (2018).
- [13] Xiyuan Lu, Gregory Moille, Anshuman Singh, Qing Li, Daron A Westly, Ashutosh Rao, Su-Peng Yu, Travis C Briles, Scott B Papp, and Kartik Srinivasan, “Milliwatt-threshold visible-telecom optical parametric oscillation using silicon nanophotonics,” *Optica* **6**, 1535–1541 (2019).
- [14] Juanjuan Lu, Ayed Al Sayem, Zheng Gong, Joshua B Surya, Chang-Ling Zou, and Hong X Tang, “Ultralow-threshold thin-film lithium niobate optical parametric oscillator,” *Optica* **8**, 539–544 (2021).
- [15] Xiyuan Lu, Gregory Moille, Ashutosh Rao, Daron A Westly, and Kartik Srinivasan, “On-chip optical parametric oscillation into the visible: generating red, orange, yellow, and green from a near-infrared pump,” *Optica* **7**, 1417–1425 (2020).
- [16] David J. Moss, Roberto Morandotti, Alexander L. Gaeta, and Michal Lipson, “New CMOS-compatible platforms based on silicon nitride and Hydex for nonlinear optics,” *Nature Photonics* **7**, 597–607 (2013).
- [17] Hyundai Park, Chong Zhang, Minh A. Tran, and Tin Komljenovic, “Heterogeneous silicon nitride photonics,” *Optica* **7**, 336 (2020).
- [18] Shun Fujii, Shuya Tanaka, Mika Fuchida, Hikaru Amano, Yuka Hayama, Ryo Suzuki, Yasuhiro Kakinuma, and Takasumi Tanabe, “Octave-wide phase-matched four-wave mixing in dispersion-engineered crystalline microresonators,” *Optics Letters* **44**, 3146–3149 (2019).
- [19] Yulong Tang, Zheng Gong, Xianwen Liu, and Hong X Tang, “Widely separated optical Kerr parametric oscillation in AlN microrings,” *Optics Letters* **45**, 1124–1127 (2020).
- [20] Renato R Domenegueti, Yun Zhao, Xingchen Ji, Marcelo Martinelli, Michal Lipson, Alexander L Gaeta, and Paulo Nussenzeig, “Parametric sideband generation in cmos-compatible oscillators from visible to telecom wavelengths,” *Optica* **8**, 316–322 (2021).
- [21] Robert W Boyd, *Nonlinear optics* (Academic press, 2020).
- [22] Gregory Moille, Qing Li, Travis C Briles, Su-Peng Yu, Tara Drake, Xiyuan Lu, Ashutosh Rao, Daron Westly, Scott B Papp, and Kartik Srinivasan, “Broadband resonator-waveguide coupling for efficient extraction of octave-spanning microcombs,” *Optics Letters* **44**, 4737–4740 (2019).
- [23] Ehsan Shah Hosseini, Siva Yegnanarayanan, Amir Hossein Atabaki, Mohammad Soltani, and Ali Adibi, “Systematic design and fabrication of high-Q single-mode pulley-coupled planar silicon nitride microdisk resonators at visible wavelengths,” *Optics Express* **18**, 2127 (2010).
- [24] Wei-Ping Huang, “Coupled-mode theory for optical waveguides: an overview,” *Journal of the Optical Society of America A* **11**, 963–983 (1994).
- [25] T Herr, V Brasch, JD Jost, I Mirgorodskiy, G Lihachev, ML Gorodetsky, and TJ Kippenberg, “Mode spectrum and temporal soliton formation in optical microres-

- onators,” *Physical Review Letters* **113**, 123901 (2014).
- [26] Sven Ramelow, Alessandro Farsi, Stéphane Clemmen, Jacob S Levy, Adrea R Johnson, Yoshitomo Okawachi, Michael RE Lamont, Michal Lipson, and Alexander L Gaeta, “Strong polarization mode coupling in microresonators,” *Optics Letters* **39**, 5134–5137 (2014).
- [27] Jordan R Stone, Gregory Moille, Xiyuan Lu, and Kartik Srinivasan, “Conversion efficiency in kerr-microresonator optical parametric oscillators: From three modes to many modes,” *Physical Review Applied* **17**, 024038 (2022).
- [28] Feng Zhou, Xiyuan Lu, Ashutosh Rao, Jordan Stone, Gregory Moille, Edgar Perez, Daron Westly, and Kartik Srinivasan, “Hybrid-mode-family kerr optical parametric oscillation for robust coherent light generation on chip,” *Laser & Photonics Reviews* , 2100582 (2022).
- [29] Xiaodong Xu, Bo Sun, Paul R Berman, Duncan G Steel, Allan S Bracker, Dan Gammon, and Lu J Sham, “Coherent optical spectroscopy of a strongly driven quantum dot,” *Science* **317**, 929–932 (2007).
- [30] Denis Viktorovich Brazhnikov, Stepan Maksimovich Ignatovich, Irina Sergeevna Mesenzova, Anton Mikailovich Mikhailov, Rodolphe Boudot, and Mikhail Nikolaevich Skvortsov, “Two-frequency sub-doppler spectroscopy of the caesium D1 line in various configurations of counter-propagating laser beams,” *Quantum Electronics* **50**, 1015 (2020).
- [31] Krishna C Balram, Daron A Westly, Marcelo Davanco, Karen E Grutter, Qing Li, Thomas Michels, Christopher H Ray, Liya Yu, Richard J Kasica, Christopher B Wallin, *et al.*, “The nanolithography toolbox,” *Journal of Research of the National Institute of Standards and Technology* **121**, 464 (2016).